Hybrid multiple-relaxation-time lattice-Boltzmann finite-difference method for axisymmetric multiphase flows

Jun-Jie Huang[1,2,5]**, Haibo Huang**[3]**, Chang Shu**[4]**, Yong Tian Chew**[4] **and Shi-Long Wang**[2]

[1] Department of Engineering Mechanics, Chongqing University, Chongqing 400044, People's Republic of China
[2] State Key Laboratory of Mechanical Transmission, Chongqing University, Chongqing 400044, People's Republic of China
[3] Department of Modern Mechanics, University of Science and Technology of China, Hefei, Anhui 230026, People's Republic of China
[4] Department of Mechanical Engineering, National University of Singapore, 9 Engineering Drive 1, Singapore 117576, Singapore

E-mail: jjhuang1980@gmail.com and jjhuang@cqu.edu.cn

Abstract
We propose a hybrid lattice-Boltzmann finite-difference method to simulate axisymmetric multiphase flows. The hydrodynamics is simulated by the lattice-Boltzmann equations with the multiple-relaxation-time (MRT) collision model and suitable forcing terms that account for the interfacial tension and axisymmetric effects. The interface dynamics is captured by the finite-difference solution of the convective Cahn–Hilliard equation. This method is applied to simulate a quiescent drop, an oscillating drop, a drop spreading on a dry surface and a drop accelerated by a constant body force. It is validated through comparisons of the computed results for these problems with analytical solutions or numerical solutions by other different methods. It is shown that the MRT-based method is able to handle more challenging cases than that with the single-relaxation-time collision model for axisymmetric multiphase flows due to its improved stability.

PACS numbers: 47.11.−j, 47.55.D−

1. Introduction

Over the last few decades, there has been substantial development in computer simulation of complex multiphase flows, which are commonly encountered in many important industries such as oil and gas, and chemical engineering, as well as in some emerging technologies such

---

[5] Author to whom any correspondence should be addressed.

as digital microfluidics. There exist mainly two types of simulation methods for multiphase flows: particle-based and continuum-based. There are two fundamental requirements for any method to simulate multiphase flows: (1) to capture/track the interface motion; (2) to capture the interfacial tension effects and their coupling with the flow. Accordingly, in a continuum formulation, two sets of equations are usually solved: one for the interface dynamics and the other for the fluid flow. For the first, well-known methods in the literature include the front-tracking [39], volume-of-fluid [33], level-set [4] and phase-field, or also known as diffuse-interface, methods [1, 19]. Among various simulation methods, the lattice-Boltzmann method (LBM) has attracted much attention due to its simplicity and superior parallel computing performance [5, 34]. One of the popular approaches in the LBM, the free-energy-based LBM [36, 35], is closely connected with the phase-field/diffuse-interface method [1]. In most free-energy-based LBMs, two sets of distribution functions (DFs) are employed to simulate the phenomena described by the two sets of equations in the continuum formulation [35, 20, 31, 25, 42, 29, 28, 6]. However, there are some issues in this approach, all of which are related to the interface equation. They have been summarized by Huang *et al* [17] and are briefly revisited next. In essence, these issues are rooted in the use of one set of independent DFs, say, g_i ($i = 0, 1, \ldots, b$), of which the total number $b + 1$ is determined by the lattice velocity model (e.g., $b + 1 = 9$ for D2Q9) and each has its evolution equation, for the interface dynamics. However, the interface dynamics may be well described by one evolution equation like the Cahn–Hilliard equation (CHE) involving *only one* independent variable, the order parameter ϕ and its derivatives (or in the common formulation, involving two related variables: ϕ and the chemical potential μ). The way to handle interfaces in the previous LBM mentioned above not only requires more memory, but also incurs a series of other issues as listed below. (1) There is the need to empirically choose the relaxation parameter for g_i (when the single-relaxation-time (SRT) collision model is used, or a set of relaxation parameters if the multiple-relaxation-time (MRT) collision model is used, as in [6]). (2) Often, there are some differences between the macroscopic equation recovered from g_i's evolution equations and the CHE, and extra efforts may be required to devise a suitable form for the equations of g_i [25, 42]. (3) There is the need to design suitable initial and boundary conditions for g_i under various conditions if different kinds of problems have to be simulated (which are not so well established as those for the lattice-Boltzmann equations (LBEs) for hydrodynamics). (4) It is not easy to use a variable mobility in the CHE using g_i within the LBM framework [20]. (5) The LBM typically uses the second-order explicit time stepping [5], which may overly limit the maximum time step for the CHE.

To overcome these issues while retaining the advantageous features of LBM, some attempts have been made to develop hybrid methods for multiphase flows. Tiribocchi *et al* [37] proposed a hybrid method for binary fluid mixtures by combining the LBM for hydrodynamics and the finite-difference method (FDM) for interface dynamics. Huang *et al* [17] developed a similar hybrid method, but with the FDM replaced by the finite-volume method; besides, they used the fourth-order Runge–Kutta method for the time stepping of the CHE.

We note that much earlier hybrid methods were developed for thermal flows with the LBM for the fluid flow and the FDM for the temperature field, for instance, by Lallemand and Luo [23], Peng *et al* [30] and Mezrhab *et al* [26]. These hybrid methods were devised to overcome some problems (spurious mode coupling and numerical instability) in the LBM for thermal flows with only one set of DFs [23, 26]. Thus, the motivation is somewhat different from that of the hybrid methods for multiphase flows. A hybrid thermal LBM has been employed to study flows in Czochralski crystal growth [30] and some other thermal flows under different configurations and conditions [26, 27]. Recently, a hybrid method has been proposed and used by Gonnella *et al* [7] and Tiribocchi *et al* [38] to simulate thermal multiphase flows with the

FDM applied for both the order parameter and the internal energy. An even more complex hybrid method has been developed by Henrich *et al* [12] for the simulation of cholesteric liquid crystals in which an order parameter *tensor* with five independent components has to be dealt with properly. In addition to the hybrid methods for flows with more physics, there is one kind of hybrid method in which conventional discretization schemes are applied for one component of the velocity, usually the azimuthal velocity component in axisymmetric flows [30, 14].

Axisymmetric flows are special cases of three-dimensional (3D) flows. The axisymmetric conditions greatly simplify the formulation and two-dimensional (2D) grids may be used for their simulation. The development and study of axisymmetric LBM have been quite active in recent years (see [9, 30, 31, 14, 32, 28, 43, 15]) because of the significant savings in computational cost when compared with a fully 3D simulation for such flows. Till now, the LBM for *axisymmetric multiphase flows* has been considered only by Premnath and Abraham [31] and by Mukherjee and Abraham [28]. Premnath and Abraham [31] used the SRT collision model, which is not as stable as the MRT model. Mukherjee and Abraham [28] extended the work by Lee and Lin [25] for flows with high density ratio and employed the MRT collision model, and were able to simulate very challenging axisymmetric multiphase flows. It is noted that they both used two sets of DFs, of which the one for interface dynamics has the above-mentioned issues and is much more complicated than the FDM for the CHE. In this paper, we propose a hybrid method that integrates the LBM for axisymmetric fluid flows with the FDM for axisymmetric interface dynamics. At present, for simplicity, we consider binary fluid mixtures with uniform density and viscosity, for which the phase-field theory is applicable and the governing equations are well established [19, 2, 41].

We would highlight that the use of conventional discretizations for the interfacial dynamics (the CHE) brings more flexibility and could improve the capability of interface capturing. Besides, further extensions of this hybrid method to multiphase flows with different densities and viscosities (to be carried out in future) require only the change of the LBM part. It is noted that in this paper, we only consider axisymmetric flows with vanishing azimuthal velocity (as in most previous works like [31, 28]).

This paper is organized as follows. In section 2, the theoretical model and the hybrid method are described in detail. In section 3, some drop problems are studied using the proposed method and the respective results are discussed. Section 4 concludes this paper.

2. Theoretical model and numerical methodology

The present method is based on the phase-field model for binary fluids. As mentioned earlier, there are two types of dynamics being considered, hydrodynamics for fluid flow and interfacial dynamics, which are closely coupled. The LBM is employed to simulate the hydrodynamics, which is usually described by the Navier–Stokes equations (NSEs), whereas the equation describing the interface motion (the CHE) is solved by the FDM for spatial discretization and the Runge–Kutta method for time marching. For convenience, the complete set of governing equations is denoted as the 'NSCH' equations. The individual components of the present method are described as follows.

2.1. Phase-field model

In the phase-field model, an order parameter ϕ is used to distinguish different fluids, and a free-energy functional is defined as

$$\mathcal{F}(\phi, \nabla\phi) = \int_V \left(\Psi(\phi) + \frac{1}{2}\kappa|\nabla\phi|^2 \right) dV + \int_S \varphi(\phi)\,dS, \tag{2.1}$$

where $\Psi(\phi)$ is the *bulk free-energy* density and takes the form

$$\Psi(\phi) = a(\phi^2 - 1)^2, \tag{2.2}$$

with a being a constant. This form indicates that ϕ varies between -1 (in one fluid) and 1 (in the other fluid). In equation (2.1), the second term is the *interfacial energy* density with κ being another constant, and the last term in the surface integral is the *surface energy* density, which takes the following form [3]:

$$\varphi(\phi_\sigma) = -\omega\phi_\sigma, \tag{2.3}$$

where ω is a parameter related to the wetting property, and ϕ_σ is the order parameter on the surface. Young's equation determines the contact angle θ_w on the wall (measured in the fluid with $\phi > 0$) as

$$\cos\theta_w = \tfrac{1}{2}[(\sqrt{1 + \tilde{\omega}})^3 - (\sqrt{1 - \tilde{\omega}})^3], \tag{2.4}$$

with the dimensionless parameter $\tilde{\omega}$ defined as

$$\tilde{\omega} = \frac{\omega}{\sqrt{2\kappa a}}. \tag{2.5}$$

The chemical potential μ is calculated by taking the variation of the free-energy functional with respect to the order parameter

$$\mu = \frac{\delta\mathcal{F}}{\delta\phi} = \frac{d\Psi(\phi)}{d\phi} - \kappa\nabla^2\phi = 4a\phi(\phi^2 - 1) - \kappa\nabla^2\phi. \tag{2.6}$$

The coefficients a and κ can be related to the interfacial tension σ and interface width W as [16]

$$a = \frac{3\sigma}{4W}, \tag{2.7}$$

$$\kappa = \frac{3\sigma W}{8}. \tag{2.8}$$

Assuming that the diffusion is driven by the chemical potential gradient, the evolution of the order parameter is governed by the convective CHE [19]:

$$\frac{\partial\phi}{\partial t} + (\boldsymbol{u} \cdot \nabla)\phi = \nabla \cdot (M\nabla\mu), \tag{2.9}$$

where M is the mobility (assumed to be constant here).

Near a solid wall, the boundary condition for the order parameter ϕ reads [3, 16]

$$\kappa\boldsymbol{n} \cdot \nabla\phi|_S = \kappa\frac{\partial\phi}{\partial n}\bigg|_S = -\omega, \tag{2.10}$$

which is simplified to be $\frac{\partial\phi}{\partial n}|_S = 0$ given a contact angle $\theta_w = 90°$. The boundary condition for the chemical potential μ is simply

$$\boldsymbol{n} \cdot \nabla\mu|_S = \frac{\partial\mu}{\partial n}\bigg|_S = 0. \tag{2.11}$$

Note that the above *zero-normal-gradient* conditions for ϕ and μ are applicable on symmetric boundaries and open boundaries (far away from the interfaces) as well.

2.2. LBM for hydrodynamics of axisymmetric flows

Before the presentation of the LBM details, it is necessary to introduce the coordinate system for axisymmetric flows and the continuum flow equations. In general, the three basic cylindrical coordinates are (r, θ, z). For axisymmetric flows, $\partial_\theta() = 0$. In this paper, since we consider only flows with vanishing azimuthal velocity (i.e. $u_\theta = 0$), the velocity vector may be written as $(u_r, 0, u_z)$. With the interfacial tension effects modeled by the phase-field model, the governing equations for the incompressible axisymmetric flows of binary fluids having uniform density and viscosity may be written as

$$\frac{\partial u_r}{\partial r} + \frac{u_r}{r} + \frac{\partial u_z}{\partial z} = 0, \tag{2.12}$$

$$\frac{\partial u_r}{\partial t} + \left(u_r \frac{\partial u_r}{\partial r} + u_z \frac{\partial u_r}{\partial z} \right) = -\frac{\partial S_p}{\partial r} + \nu \left(\frac{\partial^2 u_r}{\partial r^2} + \frac{1}{r} \frac{\partial u_r}{\partial r} + \frac{\partial^2 u_r}{\partial z^2} - \frac{u_r}{r^2} \right) - \phi \frac{\partial \mu}{\partial r}, \tag{2.13}$$

$$\frac{\partial u_z}{\partial t} + \left(u_r \frac{\partial u_z}{\partial r} + u_z \frac{\partial u_z}{\partial z} \right) = -\frac{\partial S_p}{\partial z} + \nu \left(\frac{\partial^2 u_z}{\partial r^2} + \frac{1}{r} \frac{\partial u_z}{\partial r} + \frac{\partial^2 u_z}{\partial z^2} \right) - \phi \frac{\partial \mu}{\partial z}, \tag{2.14}$$

where S_p is a term similar to the hydrodynamic pressure in the single-phase incompressible flow [19]. Here in order to use the usual notation for 2D Cartesian coordinates, we replace (z, r) with (x, y). Correspondingly, (u_z, u_r) are replaced by (u_x, u_y) (or (u, v); for convenience, both notations may be used in the following). Note that r is always *non-negative* in cylindrical coordinates, whereas y could have negative values in Cartesian coordinates. Due to symmetry, we consider only half of the domain with y being non-negative.

2.2.1. LBM with SRT. The LBM is employed to simulate the hydrodynamics described by the above governing equations, i.e. equations (2.12)–(2.14). First, the LBEs with SRT are described. As mentioned before, there have been quite a few recent works on the LBM for axisymmetric flows. Several axisymmetric LBMs have been studied and compared by Huang and Lu [15] for the simulation of single-phase flows. It was found that those models are similar in accuracy (second-order accurate), whereas the model by Zhou [43] has the best stability among them. Not aiming to compare various models again in the context of multiphase flow simulation, we adopt the specific form of source and forcing terms to mimic the axisymmetric effects by Zhou [43]. Another issue is on how to apply the forcing (and source) terms. Very early, one of the simplest forms was given by He *et al* [11] (note that, in our understanding, Zhou actually used this form in his work [43] though he presented a somewhat different form, the so-called centered scheme, with different interpretations). Later, Guo *et al* analyzed the discrete lattice effects in various forms of forcing scheme and proposed a formulation that minimizes such effects [8]. It has been widely adopted in the literature (e.g., see [6, 7]). Recently, a dedicated study on the forcing term in single-phase and multiphase LBMs has been carried out by Huang *et al* [13]. We do not intend to investigate so many forcing schemes in this work. But, in view of their popularity, we consider the two ways to apply the forcing (and source) terms mentioned above. For convenience, the one according to He *et al* [11] is denoted as 'centered' (following Zhou [43]), and the other by Guo *et al* [8] is denoted as 'GZS' based on the first letters of the authors' last names (Guo, Zheng and Shi).

With the 'centered' formulation, the LBEs with appropriate forcing for the axisymmetric effects and the interfacial tension effects are given by [43, 15]

$$f_i(\boldsymbol{x} + \boldsymbol{e}_i \delta_t, t + \delta_t) - f_i(\boldsymbol{x}, t) = -\frac{1}{\tau_f}[f_i(\boldsymbol{x}, t) - f_i^{\text{eq}}(\boldsymbol{x}, t)] + \delta_t S_i|_{(\boldsymbol{x} + \frac{1}{2}\boldsymbol{e}_i \delta_t, t + \frac{1}{2}\delta_t)}$$
$$+ \delta_t \frac{1}{c_s^2} w_i \boldsymbol{e}_i \cdot \boldsymbol{F}_{\text{ST}}|_{(\boldsymbol{x} + \frac{1}{2}\boldsymbol{e}_i \delta_t, t + \frac{1}{2}\delta_t)}, \tag{2.15}$$

where e_i $(i = 0, 1, \ldots, b)$ is the lattice velocity (for the D2Q9 model used here [22], $b = 8$),

$$
e_i = \begin{cases}
(0, 0) & \text{for } i = 0, \\
\left(\cos\left[\dfrac{(i-1)\pi}{2} \right], \sin\left[\dfrac{(i-1)\pi}{2} \right] \right) c & \text{for } i = 1, 2, 3, 4, \\
\left(\cos\left[\dfrac{(2i-9)\pi}{4} \right], \sin\left[\dfrac{(2i-9)\pi}{4} \right] \right) c & \text{for } i = 5, 6, 7, 8,
\end{cases}
\tag{2.16}
$$

with c being the lattice velocity, δ_t the time step ($\delta_x = c\delta_t$ is the grid spacing), c_s the *LBM sound speed* ($c_s = c/\sqrt{3}$ for D2Q9) and w_i the weight for different lattice velocities:

$$
w_i = \begin{cases}
\frac{4}{9} & \text{for } i = 0, \\
\frac{1}{9} & \text{for } i = 1, 2, 3, 4, \\
\frac{1}{36} & \text{for } i = 5, 6, 7, 8.
\end{cases}
\tag{2.17}
$$

S_i contains the source terms to account for the axisymmetric effects, and it is given by [43, 15]

$$
S_i = S_i^{(1)} + S_i^{(2)}, \quad S_i^{(1)} = w_i S = -w_i \frac{\rho u_y}{y}, \quad S_i^{(2)} = \frac{1}{c_s^2} w_i e_i \cdot F_{\text{axisym}},
\tag{2.18}
$$

where S is a source term to account for the change in the continuity equation, ρ is the density (nearly a constant) and F_{axisym} is the virtual 'force' to mimic the axisymmetric effects:

$$
F_{\text{axisym}} = (F_{\text{axisym},x}, F_{\text{axisym},y}) = \left(\frac{-\rho u_x u_y}{y} + \frac{\rho \nu}{y} \frac{\partial u_x}{\partial y}, \frac{-\rho u_y u_y}{y} + \frac{\rho \nu}{y} \left(\frac{\partial u_y}{\partial y} - \frac{u_y}{y} \right) \right).
\tag{2.19}
$$

In equation (2.15), F_{ST} accounts for the interfacial tension effects and takes the form

$$
F_{\text{ST}} = -\phi \nabla \mu.
\tag{2.20}
$$

The equilibrium DF f_i^{eq} is

$$
f_i^{\text{eq}} = w_i \left\{ \rho + \rho \left[\frac{1}{c_s^2} e_i \cdot u + \frac{1}{2c_s^4} (e_i \otimes e_i - c_s^2 \mathbf{I}) : (u \otimes u) \right] \right\}.
\tag{2.21}
$$

The subscript in equation (2.15), $|_{(x + \frac{1}{2} e_i \delta_t, t + \frac{1}{2}\delta_t)}$, denotes that the respective terms take their values at the position $x + \frac{1}{2} e_i \delta_t$ and time $t + \frac{1}{2}\delta_t$. It should be noted that in this 'centered' scheme, the evolution equations are in fact still explicit because in the Chapman–Enskog expansion, the high-order terms may be neglected [15, 43]. The final formulation coincides with that given in [16]. The second-order moments of f_i^{eq} satisfy the following relation:

$$
\sum_{i=0}^{b} e_{i_\alpha} e_{i_\beta} f_i^{\text{eq}} = \rho u_\alpha u_\beta + S_p \delta_{\alpha\beta},
\tag{2.22}
$$

where $S_p = \rho c_s^2$. The density and momentum are calculated from the zeroth- and first-order moments of f_i:

$$
\rho = \sum_{i=0}^{b} f_i, \quad \rho u = \sum_{i=1}^{b} f_i e_i.
\tag{2.23}
$$

For very small *LBM Mach number* $M_{\text{LBM}} = \frac{|u|_{\max}}{c_s}$ ($|u|_{\max}$ is the maximum velocity magnitude), the density ρ varies slightly around a constant value. By the Chapman–Enskog expansion, equations (2.12)–(2.14) can be obtained in the long-time, large-wavelength limit with the kinematic viscosity ν related to the relaxation parameter τ_f as

$$
\nu = c_s^2 (\tau_f - 0.5) \delta_t.
\tag{2.24}
$$

In practice, the LBEs are implemented through two steps: collision and streaming. Specifically, equation (2.15) is split as

$$f_i(\boldsymbol{x}, t^+) = f_i(\boldsymbol{x}, t) - \frac{1}{\tau_f}\Big[f_i(\boldsymbol{x}, t) - f_i^{\text{eq}}(\boldsymbol{x}, t)\Big] + \delta_t S_i + \delta_t \frac{1}{c_s^2} w_i \boldsymbol{e}_i \cdot \boldsymbol{F}_{\text{ST}}, \quad (2.25)$$

$$f_i(\boldsymbol{x} + \boldsymbol{e}_i \delta_t, t + \delta_t) = f_i(\boldsymbol{x}, t^+), \quad (2.26)$$

of which the first step is completely local and the second simply involves the propagation of the post-collision DF to the respective neighbor according to the lattice velocity.

The 'GZS' formulation is different from the 'centered' one mainly in two aspects: one is the form of the forcing terms and the other is the calculation of the macroscopic variables. Besides the method given in the original paper by Guo *et al* [8], the 'GZS' formulation may also be derived by integrating the discrete Boltzmann equations (with forcing terms) in time with the second-order trapezoidal approximation for the collision and forcing terms, together with a re-definition of the DFs [15]. Specifically, it contains the following formulas for the evolution equations and macroscopic variables [8, 15, 6],

$$f_i(\boldsymbol{x} + \boldsymbol{e}_i \delta_t, t + \delta_t) - f_i(\boldsymbol{x}, t) = -\frac{1}{\tau_f}[f_i(\boldsymbol{x}, t) - f_i^{\text{eq}}(\boldsymbol{x}, t)] + \left(1 - \frac{1}{2\tau_f}\right)\delta_t w_i S$$

$$+ \left(1 - \frac{1}{2\tau_f}\right)\delta_t \frac{1}{c_s^2} w_i \left[(\boldsymbol{e}_i - \boldsymbol{u}) + \frac{\boldsymbol{e}_i \cdot \boldsymbol{u}}{c_s^2}\boldsymbol{e}_i\right] \cdot (\boldsymbol{F}_{\text{axisym}} + \boldsymbol{F}_{\text{ST}}), \quad (2.27)$$

$$\rho = \sum_{i=0}^{b} f_i + \frac{1}{2}\delta_t S, \quad \rho\boldsymbol{u} = \sum_{i=1}^{b} f_i \boldsymbol{e}_i + \frac{1}{2}\delta_t(\boldsymbol{F}_{\text{axisym}} + \boldsymbol{F}_{\text{ST}}). \quad (2.28)$$

From the above, it is seen that the 'GZS' formulation appears to be a bit more complicated than the 'centered' one.

Near a solid wall, the bounce-back-by-link (BBL, also known as *half-way wall bounce-back*) condition is applied for f_i [11, 44, 34]. In this work, two other boundary conditions are also encountered, namely the free slip and periodic boundary conditions. The details about them may be found in [34].

2.2.2. LBM with MRT. It is known in the literature that the LBM with SRT is not so stable at high Reynolds numbers as the LBM with MRT. To have a better stability property, one can employ the MRT-LBM. The present MRT-LBM follows that proposed by Lallemand and Luo [22]. In the MRT-LBM, the collision step in the LBEs is carried out in the moment space spanned by the moments (kinetic modes) formed through some properly chosen transformations of the DFs, containing the density and momentum.

When no source terms are present, the evolution equations of the DFs in the MRT-LBM are given as [22]

$$|f(\boldsymbol{x} + \boldsymbol{e}_i \delta_t, t + \delta_t)\rangle - |f(\boldsymbol{x}, t)\rangle = -\mathbf{S}[|f(\boldsymbol{x}, t)\rangle - |f^{\text{eq}}(\boldsymbol{x}, t)\rangle], \quad (2.29)$$

where $\mathbf{S}$ is the collision matrix, $|()\rangle$ denotes the column vector, for instance,

$$|f(\boldsymbol{x}, t)\rangle = (f_0(\boldsymbol{x}, t), f_1(\boldsymbol{x}, t), \dots, f_b(\boldsymbol{x}, t))^T. \quad (2.30)$$

The moments are given by

$$m_j = \langle\phi_j|f\rangle = \langle f|\phi_j\rangle, \quad (j = 0, 1, \dots, b), \quad (2.31)$$

where $|\phi_j\rangle$ is an orthogonal basis set constructed from polynomials of some vectors related to the lattice velocity $\boldsymbol{e}_i$. Using the above transformations, the evolution equations can be written as

$$|f(\boldsymbol{x} + \boldsymbol{e}_i \delta_t, t + \delta_t)\rangle - |f(\boldsymbol{x}, t)\rangle = -\mathbf{M}^{-1}\mathbf{S}[|m(\boldsymbol{x}, t)\rangle - |m^{\text{eq}}(\boldsymbol{x}, t)\rangle], \quad (2.32)$$

where the matrix $\mathbf{M}$ represents the transformation from the DF space to the moment space ($\mathbf{M}^{-1}$ is the inverse transformation), and m^{eq} are the equilibrium moments.

For the D2Q9 velocity model used here, the transformation matrix $\mathbf{M}$ is [22]

$$\mathbf{M} = \begin{bmatrix} 1 & 1 & 1 & 1 & 1 & 1 & 1 & 1 & 1 \\ -4 & -1 & -1 & -1 & -1 & 2 & 2 & 2 & 2 \\ 4 & -2 & -2 & -2 & -2 & 1 & 1 & 1 & 1 \\ 0 & 1 & 0 & -1 & 0 & 1 & -1 & -1 & 1 \\ 0 & -2 & 0 & 2 & 0 & 1 & -1 & -1 & 1 \\ 0 & 0 & 1 & 0 & -1 & 1 & 1 & -1 & -1 \\ 0 & 0 & -2 & 0 & 2 & 1 & 1 & -1 & -1 \\ 0 & 1 & -1 & 1 & -1 & 0 & 0 & 0 & 0 \\ 0 & 0 & 0 & 0 & 0 & 1 & -1 & 1 & -1 \end{bmatrix}. \tag{2.33}$$

The corresponding nine moments are [22]

$$|m\rangle = (\rho, e, \varepsilon, j_x, q_x, j_y, q_y, p_{xx}, p_{xy})^T, \tag{2.34}$$

where e is related to the energy, ε is related to the energy square, j_x and j_y are the x- and y-components of the momentum, q_x and q_y are related to the x- and y-components of the energy flux and p_{xx} and p_{xy} are related to the stress tensor. Up to second order in ρ, j_x and j_y, the equilibria of the non-conserved moments are given by

$$e^{(\mathrm{eq})} = -2\rho + 3\left(j_x^2 + j_y^2\right), \tag{2.35}$$

$$\varepsilon^{(\mathrm{eq})} = \rho - 3\left(j_x^2 + j_y^2\right), \tag{2.36}$$

$$q_x^{(\mathrm{eq})} = -j_x, \tag{2.37}$$

$$q_y^{(\mathrm{eq})} = -j_y, \tag{2.38}$$

$$p_{xx}^{(\mathrm{eq})} = \left(j_x^2 - j_y^2\right), \tag{2.39}$$

$$p_{xy}^{(\mathrm{eq})} = j_x j_y. \tag{2.40}$$

The diagonal collision matrix $\mathbf{S}$ is

$$\mathbf{S} = \mathrm{diag}(0, -s_1, -s_2, 0, -s_4, 0, -s_6, -s_7, -s_8), \tag{2.41}$$

where s_2, s_4 and s_6 can be adjusted with no effects on the transport coefficients (to second order in the wavenumber), s_1 determines the bulk viscosity and $s_7 = s_8 = \frac{1}{\tau_f}$ determines the shear viscosity [22]. Based on the guidelines and suggestions in [22], we use the following values for the adjustable relaxation parameters: $s_1 = 1.5$, $s_2 = s_4 = s_6 = 1.1$. Note that they are not uniquely determined, but the study of their effects on the results (hopefully to be small as long as they are within the ranges given in [22]) is out of the scope of this paper.

Next, the source and forcing terms are considered. In general, they may be added either into the moment space or directly into the equations for the DFs (as in equation (2.15)). In this work, they are applied in the moment space. For the 'centered' formulation and the D2Q9 velocity model, the column vector in the moment space corresponding to the source term (for continuity equation) reads

$$[S, -2S, S, 0, 0, 0, 0, 0, 0]^T, \tag{2.42}$$

and that corresponding to the (total) forcing term reads

$$[0, 0, 0, F_{T,x}, -F_{T,x}, F_{T,y}, -F_{T,y}, 0, 0]^T, \tag{2.43}$$

with $F_{T,x}$ and $F_{T,y}$ being the x- and y-components of the total force $\boldsymbol{F}_T$ ($= \boldsymbol{F}_{\text{axisym}} + \boldsymbol{F}_{\text{ST}}$). For the 'GZS' formulation, the column vector corresponding to the source term reads

$$[S, (1 - 0.5s_1)(-2S), (1 - 0.5s_2)S, 0, 0, 0, 0, 0]^T, \tag{2.44}$$

and that corresponding to the forcing terms reads [6]

$$\begin{bmatrix} 0 \\ 6(1 - 0.5s_1)(\boldsymbol{u} \cdot \boldsymbol{F}_T) \\ -6(1 - 0.5s_2)(\boldsymbol{u} \cdot \boldsymbol{F}_T) \\ (1 - 0.5s_3)F_{T,x} \\ -(1 - 0.5s_4)F_{T,x} \\ (1 - 0.5s_5)F_{T,y} \\ -(1 - 0.5s_6)F_{T,y} \\ 2(1 - 0.5s_7)(u_x F_{T,x} - u_y F_{T,y}) \\ (1 - 0.5s_8)(u_x F_{T,y} + u_y F_{T,x}) \end{bmatrix}. \tag{2.45}$$

Besides, the density and momentum components (ρ, j_x and j_y) in equations (2.35)–(2.40) are now computed from equation (2.28). It is seen that in the MRT-LBM, the 'GZS' formulation is even more complicated than the 'centered' one (as compared with the situation in the SRT-LBM).

We have found that for typical case studies (to be presented later), the results computed by the 'GZS' and 'centered' formulations have only very small differences (some comparisons will be given later). Thus, we prefer using the 'centered' formulation (i.e. the simpler one), and it is the *default* choice in this work.

In the MRT-LBM, the LBEs are implemented in two steps similar to those in the SRT-LBM except that the collision step is performed in the moment space. It involves first the transformation of the DFs to the moments, then the relaxation for each moment, and finally the transformation of the moments back to the DFs. The streaming step remains unchanged.

2.3. Finite-difference method for interface dynamics

As described in section 2.1, the interface dynamics is modeled through the order parameter field governed by the CHE, i.e. equation (2.9). Note that equation (2.6) is required to calculate the chemical potential in equation (2.9). Using the notations for cylindrical coordinates in section 2.2, the CHE for axisymmetric flows may be written as

$$\frac{\partial \phi}{\partial t} + \left(u \frac{\partial \phi}{\partial x} + v \frac{\partial \phi}{\partial y} \right) = M \nabla^2_{\text{axisym}} \mu, \tag{2.46}$$

where the Laplacian of μ in cylindrical coordinates is

$$\nabla^2_{\text{axisym}} \mu = \frac{\partial^2 \mu}{\partial y^2} + \frac{1}{y} \frac{\partial \mu}{\partial y} + \frac{\partial^2 \mu}{\partial x^2}. \tag{2.47}$$

Similarly, in cylindrical coordinates, the chemical potential can be written as

$$\mu = 4a\phi(\phi^2 - 1) - \kappa \left(\frac{\partial^2 \phi}{\partial y^2} + \frac{1}{y} \frac{\partial \phi}{\partial y} + \frac{\partial^2 \phi}{\partial x^2} \right). \tag{2.48}$$

In the present hybrid method, the phase-field variables (including ϕ and μ) are defined on the same grid points as the DFs f_i, and they are updated at the same time segments (i.e. $t = 0$, δ_t, $2\delta_t$,...). Therefore, the coupling between the hydrodynamics and interfacial dynamics is relatively straightforward.

2.3.1. Spatial discretization. For the evaluation of the derivatives of phase-field variables, two types of schemes have been tried: (1) the common second-order centered scheme (denoted as 2nd); (2) a scheme based on the D2Q9 velocity model which has better isotropic properties and is also second-order accurate (denoted as iso). When the 2nd scheme is used, the first derivatives and the (usual) Laplacian (in Cartesian coordinates) of ϕ are calculated as

$$\frac{\partial \phi}{\partial x} = \frac{1}{2\delta_x}[\phi(\boldsymbol{x} + \boldsymbol{e}_1\delta_t) - \phi(\boldsymbol{x} + \boldsymbol{e}_3\delta_t)], \tag{2.49}$$

$$\frac{\partial \phi}{\partial y} = \frac{1}{2\delta_x}[\phi(\boldsymbol{x} + \boldsymbol{e}_2\delta_t) - \phi(\boldsymbol{x} + \boldsymbol{e}_4\delta_t)], \tag{2.50}$$

$$\frac{\partial^2 \phi}{\partial x^2} + \frac{\partial^2 \phi}{\partial y^2} = \frac{1}{\delta_x^2}[\phi(\boldsymbol{x} + \boldsymbol{e}_1\delta_t) + \phi(\boldsymbol{x} + \boldsymbol{e}_3\delta_t) + \phi(\boldsymbol{x} + \boldsymbol{e}_2\delta_t) + \phi(\boldsymbol{x} + \boldsymbol{e}_4\delta_t) - 4\phi(\boldsymbol{x})]. \tag{2.51}$$

When the iso scheme is used, the derivatives are obtained as

$$\frac{\partial \phi}{\partial x} = \frac{3}{c\delta_x} \sum_{i=1}^{8} w_i e_{ix} \phi(\boldsymbol{x} + \boldsymbol{e}_i\delta_t), \tag{2.52}$$

$$\frac{\partial \phi}{\partial y} = \frac{3}{c\delta_x} \sum_{i=1}^{8} w_i e_{iy} \phi(\boldsymbol{x} + \boldsymbol{e}_i\delta_t), \tag{2.53}$$

$$\frac{\partial^2 \phi}{\partial x^2} + \frac{\partial^2 \phi}{\partial y^2} = \frac{6}{\delta_x^2} \left[\sum_{i=1}^{8} w_i \phi(\boldsymbol{x} + \boldsymbol{e}_i\delta_t) - (1 - w_0)\phi(\boldsymbol{x}) \right]. \tag{2.54}$$

It is noted that the above two types of formulas are used to evaluate the derivatives in $\boldsymbol{F}_{\mathrm{ST}}$ in the source term of LBEs as well, but the derivatives in $\boldsymbol{F}_{\mathrm{axisym}}$ (specifically, $\frac{\partial u}{\partial y}$ and $\frac{\partial v}{\partial y}$) are simply calculated by the common second-order centered schemes since the velocity field is relatively smooth.

In some previous studies, the iso scheme was found to be able to reduce the spurious velocity in the interfacial region of multiphase flows [37]. However, there are some differences between this work and that by Tiribocchi *et al* [37], in which the iso scheme was applied to evaluate the derivatives in the LBEs and not in the CHE. In addition, Tiribocchi *et al* used the first-order upwind scheme to discretize the convective terms in the CHE [37], which has a lower order of accuracy and larger numerical dissipation (though the stability is improved). We will make some comparisons between the 2nd and iso schemes for certain cases under the current implementation. Note that for most of the problems studied in this work, the default derivative evaluation scheme is the iso scheme.

2.3.2. Temporal discretization. Substituting either of the above two sets of formulas into equation (2.46), one obtains its semi-discrete form which may be compactly written as

$$\frac{\mathrm{d}\phi}{\mathrm{d}t} \equiv L(\phi), \tag{2.55}$$

where the right-hand side contains all the discretized spatial derivatives. In this work, the time stepping employs the explicit fourth-order Runge–Kutta method. Note that the velocity field is frozen during the time marching of the CHE from t^n to $t^{n+1} (= t^n + \delta_t)$. Specifically, the time stepping follows these steps:

$$\begin{aligned}
a^n &= \delta_t L(t^n, \phi^n), \\
b^n &= \delta_t L\left(t^n + \tfrac{1}{2}\delta_t, \phi^n + \tfrac{1}{2}a^n\right), \\
c^n &= \delta_t L\left(t^n + \tfrac{1}{2}\delta_t, \phi^n + \tfrac{1}{2}b^n\right), \\
d^n &= \delta_t L\left(t^n + \delta_t, \phi^n + c^n\right),
\end{aligned} \tag{2.56}$$

$$\phi^{n+1} = \phi^n + \tfrac{1}{6}(a^n + 2b^n + 2c^n + d^n). \tag{2.57}$$

2.4. Time marching of the coupled system

Equations (2.15), (2.46) and (2.48) form a coupled system (when the SRT-LBM is used; for the MRT-LBM, equation (2.15) is replaced by the relevant equations in section 2.2.2). The time marching of this system is essential to obtain the main variables at t^{n+1} from those at t^n:

$$(\rho^n, u^n, v^n, f_i^n; \phi^n, \mu^n) \rightarrow (\rho^{n+1}, u^{n+1}, v^{n+1}, f_i^{n+1}; \phi^{n+1}, \mu^{n+1}). \tag{2.58}$$

One can do the time marching for the CHE first, i.e. to obtain ϕ^{n+1}, μ^{n+1} by using equations (2.56) and (2.57) (u^n, v^n are fixed at this stage), and then carry out the LBM steps (for instance, when SRT is used, equations (2.25) and (2.26) are applied with ϕ^{n+1}, μ^{n+1} being used to evaluate the interfacial tension force in equation (2.25)). Instead, one can also do the time marching for the LBEs first and then that for the CHE. Some numerical tests show that the change of the order does not affect the results in a significant way. Here, we adopt the former.

2.5. Remarks on the advantages of hybrid method

By directly discretizing the CHE, the hybrid method overcomes the problems with the LBM using two sets of DFs mentioned in section 1 while keeping some important advantages of LBM (e.g., no need to solve the Poisson equation for the (hydrodynamic) pressure). Specifically, it is advantageous because all the issues related to g_i for the interfacial dynamics are no longer present:

- It avoids the need to adjust the empirical relaxation parameter(s) for the DFs g_i.
- The CHE is approximated with the spatial and temporal accuracies suitably controlled.
- The initial and boundary conditions for the phase-field variables (ϕ and μ) are easily applied accurately.
- The time stepping for the CHE is more flexible: for instance, schemes with better stability properties like high-order Runge–Kutta schemes (or even semi-implicit schemes) may be used.
- It is easier to use a variable mobility $M(\phi)$ (i.e. a mobility dependent on the order parameter).

Besides, the hybrid framework allows easier inclusion of more physical phenomena, for example, the heat equation in thermal flows (e.g., [38]). Note that the fourth aspect about the time stepping becomes more important as the interfacial thickness W (reflected by the Cahn number Cn to be defined later) decreases because the CHE becomes stiffer at smaller Cn.

3. Results and discussions

3.1. Characteristic quantities, dimensionless numbers and common setup

Before presenting the results for a series of different test problems, we introduce the common characteristic quantities and dimensionless numbers. In each problem, there is a drop of radius R, which is chosen to be the characteristic length L_c. The constant density is selected as the characteristic density ρ_c. The interfacial tension is σ and the kinematic viscosity is ν (thus, the dynamic viscosity is $\mu = \rho_c \nu$). No body force is included except for the last problem. Following [21], we use a characteristic velocity U_c defined as follows:

$$U_c = \frac{\sigma}{\rho_c \nu}. \tag{3.1}$$

Then, the characteristic time T_c is

$$T_c = \frac{L_c}{U_c} = \frac{R\rho_c\nu}{\sigma}. \tag{3.2}$$

Note that all quantities of length, time and velocity below are scaled by L_c, T_c and U_c, respectively (unless otherwise specified). With the above definitions of characteristic quantities, the capillary number is given by

$$Ca = \frac{\rho_c\nu U_c}{\sigma} = 1, \tag{3.3}$$

and the Reynolds number by

$$Re = \frac{U_c R}{\nu} = \frac{\sigma}{\rho_c\nu}\frac{R}{\nu} = \frac{\sigma R}{\rho_c\nu^2}. \tag{3.4}$$

It should be noted that the capillary number and the Reynolds number defined in this way do not reflect the *actual* physics of the problem due to the velocity scale specifically selected, but they are helpful in setting up the simulation.

In the phase-field model, two additional parameters are introduced: (1) the Cahn number, defined to be the ratio of interface width over the characteristic length,

$$Cn = \frac{W}{L_c}, \tag{3.5}$$

and, (2) the Peclet number, which reflects the ratio of convection over diffusion in the CHE,

$$Pe = \frac{U_c L_c^2}{M\sigma}. \tag{3.6}$$

Some previous studies have investigated or discussed the issue on how to choose these two parameters to obtain reliable results for different problems [19, 41]. But it is not a major concern here since we mainly focus on the numerical method and implementation. In this work, these two parameters are picked in such a way that the proposed method may be verified through comparisons with known laws or other methods using relatively low computational cost.

The domain of simulation is a rectangle specified by $0 \leqslant x \leqslant L_x$, $0 \leqslant y \leqslant L_y$. In all problems, the lower side is the symmetric axis on which the symmetric boundary conditions are applied. In other words, all of the problems considered are within a cylindrical tube and the domain is half of its cross-section passing through its axis. In the first several problems, we assume that there are solid walls on the upper, left and right sides, where the BBL boundary conditions are used for f_i. Besides, the contact angles of all walls are assumed to be $\theta_w = 90°$. Thus, the *zero-normal-gradient* condition is applied for both ϕ and μ. In the last problem, the boundaries on the upper, left and right sides are different and the details will be described later. The initial position of the drop center is (x_c, y_c).

In the LBM, the lattice units are usually used. For example, δ_x, δ_t and c are the lattice units for length, time and velocity variables in the LBM, respectively (see section 2.2). They are related to the above characteristic quantities and the spatial and temporal discretizations. Suppose the characteristic length L_c is discretized by N_x uniform segments and the characteristic time T_c is discretized by N_t uniform segments, then one has

$$\delta_x = \frac{L_c}{N_x}, \quad \delta_t = \frac{T_c}{N_t}. \tag{3.7}$$

The lattice velocity c is obtained as $c = \delta_x/\delta_t$. But note that the lattice units are not used in the following. We just intend to clarify the connections between two different scaling systems.

3.2. Quiescent drop

First, an initially spherical quiescent drop is considered. For this case, no significant macroscopic flows are present. The common physical parameter is $Ca = 1$, the domain size is $L_x \times L_y = 4 \times 2$, the center of the drop is $(x_c, y_c) = (L_x/2, 0) = (2, 0)$ and the numerical parameters are $Cn = 0.2$, $N_x = 20$, $N_t = 80$. Note that N_x is the parameter to discretize the characteristic length (here the drop radius R, not the domain length L_x). The Reynolds number takes one of the following values: 1×10^3, 1×10^4 and 1×10^5, the Peclet number may be 2×10^3 or 4×10^3. This problem is useful for us to examine some fundamental Cahn–Hilliard dynamics as explained next.

3.2.1. Initial condition and evolution toward equilibrium. In the present cylindrical coordinates, using the above notations, the initial order parameter field for a spherical drop of radius R with its center at (x_c, y_c) is specified as

$$\phi(r_d) = -\tanh\left(\frac{2(r_d - R)}{W}\right), \tag{3.8}$$

where $r_d = \sqrt{(x - x_c)^2 + (y - y_c)^2}$ is the distance away from the drop center. This order parameter field does not correspond to the equilibrium condition for an interface with a finite curvature. Driven mainly by the diffusion in the CHE, the exchange between interfacial and bulk energies occurs [40] and the order parameter field evolves spontaneously toward the *true* equilibrium state with the order parameters inside and outside the drop being $\phi_{\text{in}}^{\text{eq}} = 1 + \epsilon_{\text{in}}^{\text{eq}}$ and $\phi_{\text{out}}^{\text{eq}} = -(1 - \epsilon_{\text{out}}^{\text{eq}})$ ($\epsilon_{\text{in}}^{\text{eq}}$ and $\epsilon_{\text{out}}^{\text{eq}}$ taking some small positive values), which satisfy the Laplace law:

$$p_{\text{in}}^t - p_{\text{out}}^t = p_{\text{in}}^b(\phi_{\text{in}}^{\text{eq}}) - p_{\text{out}}^b(\phi_{\text{out}}^{\text{eq}}) = \frac{\sigma}{2R_d^{\text{eq}}}, \tag{3.9}$$

where p^b is the *bulk pressure* related to ϕ through the *equation of state*,

$$p^b = \phi \frac{\mathrm{d}\Psi(\phi)}{\mathrm{d}\phi} - \Psi(\phi), \tag{3.10}$$

and p^t is the *total* pressure related to p^b as

$$p^t = S_p + p^b - \left(\kappa\phi\nabla^2\phi - \tfrac{1}{2}\kappa|\nabla\phi|^2\right). \tag{3.11}$$

During this process, the drop shrinks a bit; thus, the drop radius in equilibrium R_d^{eq} is slightly smaller than the initial radius R. We note that this problem has been investigated systematically by Yue *et al* [40]. Here, we use this problem for the validation of the present method and also for comparing different schemes or methods.

From equation (3.9), assuming a quasi-equilibrium state at each moment, one can calculate an evolving interfacial tension as

$$\sigma_{\text{num}}(t) = 2R_d(t)\left(p_{\text{in}}^b(\phi_{\text{in}}(t)) - p_{\text{out}}^b(\phi_{\text{out}}(t))\right), \tag{3.12}$$

where the order parameters inside and outside the drop (ϕ_{in} and ϕ_{out}), and the drop radius R_d are all functions of time. In this work, ϕ_{in} and ϕ_{out} were sampled at the drop center and some point that is $R_d + 2Cn$ away from the center, respectively, so that both are outside the interfacial region. Assuming that the drop shrinks isotropically, one can find R_d by simply measuring the radius along the x-axis R_x. In practice, we also measured the radius in the y-direction along the middle vertical line R_y. The temporal variation of R_y was found to agree with that of R_x well (only very small differences were observed), and R_d was taken as $(R_x + R_y)/2$. In order

13
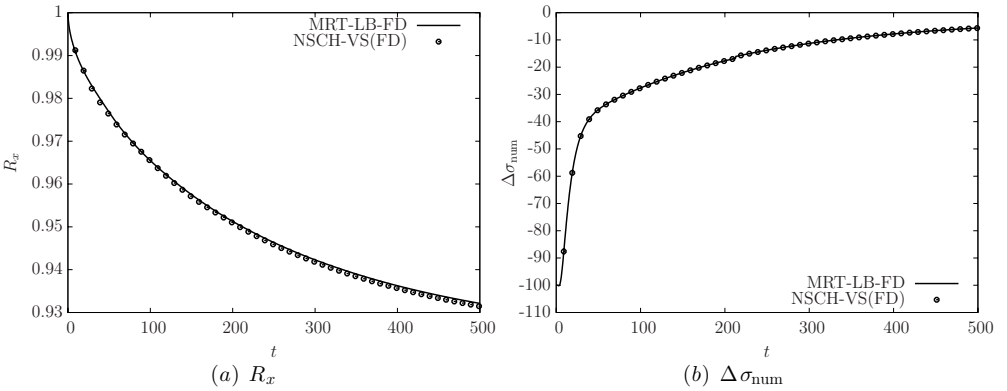
Figure 1. Comparison of the evolutions of (*a*) the drop radius on the *x*-axis R_x and (*b*) the relative deviation of the numerically measured interfacial tension $\Delta\sigma_{num}$ (in per cent) by MRT-LB-FD and NSCH-VS(FD) with $Re = 1 \times 10^3$, $Ca = 1$, $Cn = 0.2$, $Pe = 4 \times 10^3$, $N_x = 20$ and $N_t = 80$.

to validate the present method, the numerically measured interfacial tension σ_{num} is compared with the theoretical one σ by checking its relative deviation defined as

$$\Delta\sigma_{num} = \frac{\sigma_{num} - \sigma}{\sigma} \times 100\%. \tag{3.13}$$

In addition, the maximum velocity magnitude $\sqrt{u^2 + v^2}|_{max}$ is monitored during simulation.

Here, we seek to verify that the present method and implementation are correct by checking certain key characteristics of the solution like $\Delta\sigma_{num}$ and/or comparing the current results with those obtained from another different method. The method used for comparison applies the FDM to directly solve the coupled NSCH equations using the vorticity-stream function formulation for the NSEs and also using staggered grids for the flow variables (i.e. the vorticity and stream function) and the phase-field variables [18]. For brevity, the present method is denoted as MRT-LB-FD and the other method is denoted as NSCH-VS(FD).

3.2.2. Comparison between two methods: MRT-LB-FD *versus* NSCH-VS(FD). We focus on one case with $Re = 1 \times 10^3$, $Ca = 1$, $Cn = 0.2$, $N_x = 20$, $N_t = 80$, $Pe = 4 \times 10^3$ first. Figure 1 shows the evolution of the drop radius on the symmetric axis R_x (figure 1(*a*)) and that of $\Delta\sigma_{num}$ (figure 1(*b*)) by the present method and by NSCH-VS(FD). It is easy to find that the two methods agree very well for the two quantities monitored. As mentioned above, the drop shrinks a bit to achieve the *true* equilibrium and it is observed in figure 1(*a*) that both methods predict that R_x decreases quickly during the initial stage, and slower and slower afterward, reaching approximately 0.93 of its initial value at $t = 500$. The change of about 7% is relatively big and is related to the relatively large value of *Cn* [40]. From figure 1(*b*), $\Delta\sigma_{num}$ obtained by either method goes toward zero as time evolves, reaching about -5.6% at $t = 500$, which indicates that the balance between the pressure and the interfacial tension is gradually achieved. Besides, it is difficult to distinguish the two results on $\Delta\sigma_{num}$ by the two different methods.

3.2.3. Comparison between two schemes: 2nd *versus* iso. In section 2.3.1, two schemes (2nd and iso) to evaluate the spatial derivatives of the phase-field variables were given, and it was noted that the default is the iso scheme. Here, we compare the two schemes for
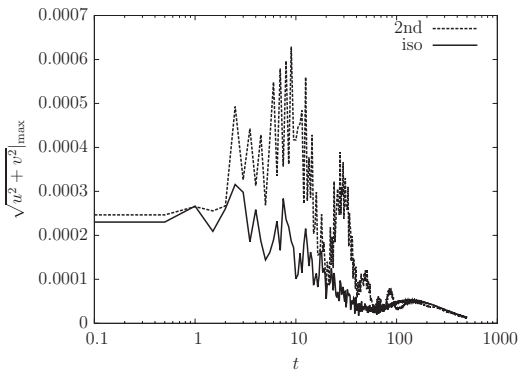
Figure 2. Comparison of the maximum velocity magnitude $\sqrt{u^2 + v^2}|_{max}$ evolutions by the `2nd` scheme and the `iso` scheme with $Re = 1 \times 10^3$, $Ca = 1$, $Cn = 0.2$, $Pe = 4 \times 10^3$, $N_x = 20$ and $N_t = 80$.

the quiescent drop problem by examining the maximum velocity magnitude $\sqrt{u^2 + v^2}|_{max}$ observed during simulation. (It has been confirmed that the two schemes give very close predictions for R_x and $\Delta\sigma_{num}$; thus, these two are not the main focus here.) Figure 2 gives the semi-logarithmic plot of $\sqrt{u^2 + v^2}|_{max}$'s evolutions by the two schemes using the same set of parameters as above. It is seen from figure 2 that $\sqrt{u^2 + v^2}|_{max}$ in general remains to be small ($O(10^{-4})$) during the whole simulation. This is expected since an initially quiescent drop is considered and there is no significant *macroscopic* flow of any kind (either imposed externally or caused by capillarity). From figure 2, one also finds that $\sqrt{u^2 + v^2}|_{max}$ shows large fluctuations initially and almost keeps decreasing after certain time. For the two schemes being compared, major differences are seen before $t = 100$, during which the fluctuation by the `2nd` scheme is much more violent than that by the `iso` scheme. The peak value of $\sqrt{u^2 + v^2}|_{max}$ by the `2nd` scheme is also much larger. These can make the `2nd` scheme less stable under more challenging numerical settings (as already encountered in some numerical tests not shown here). We note that the `iso` scheme costs (slightly) more computation time, but its improved stability makes it a worthy choice.

3.2.4. Comparison between two collision models: MRT versus SRT. Next, we study the MRT- and SRT-based hybrid methods described in sections 2.2.1 and 2.2.2, respectively. We still focus on the maximum velocity magnitude $\sqrt{u^2 + v^2}|_{max}$ in the simulation of a quiescent drop. It should be noted that in diverged simulations below, the expected final equilibrium state could not be reached. Figure 3 gives the logarithmic plots of the evolutions of $\sqrt{u^2 + v^2}|_{max}$ at three Reynolds numbers, $Re = 1 \times 10^3$, 1×10^4, 1×10^5, using the two collision models. The Peclet number is $Pe = 2 \times 10^3$, whereas all other parameters are the same as above. It is seen that for all the Reynolds numbers, $\sqrt{u^2 + v^2}|_{max}$ by SRT is larger than that by MRT (though only slightly when the computation is stable). At large Reynolds numbers ($Re = 1 \times 10^4$, 1×10^5), the computation using SRT becomes unstable quickly, as reflected from the abruptly increasing $\sqrt{u^2 + v^2}|_{max}$ (exceeding 0.1 at around $t = 30$ for $Re = 1 \times 10^5$ and at around $t = 46$ for $Re = 1 \times 10^4$); the larger the Re is, the earlier the instability occurs. By contrast, the computation using MRT remains stable in all cases.

3.3. Oscillating drop

In the second problem, we consider an initially deformed static drop specified by a prolate spheroid having a minimum radius R_{min} (in the direction perpendicular to the axis) and a
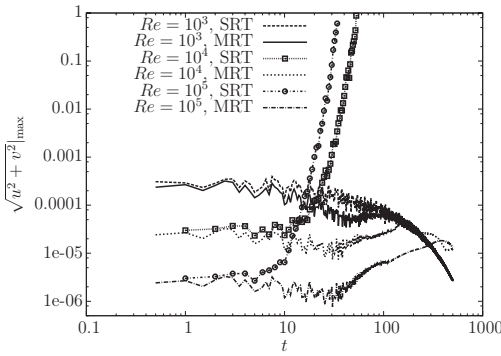
Figure 3. Comparison of the maximum velocity magnitude $\sqrt{u^2 + v^2}|_{\max}$ evolutions by the SRT-and MRT-based hybrid LB-FD method at $Re = 1 \times 10^3$, 1×10^4, 1×10^5, with $Ca = 1$, $Cn = 0.2$, $Pe = 2 \times 10^3$, $N_x = 20$ and $N_t = 80$.

maximum radius $R_{\max}$ (along the axis). $R_{\min}$ and $R_{\max}$ are related to the equilibrium radius R_d (when the drop becomes spherical) as

$$R_d^3 = R_{\min}^2 R_{\max}. \tag{3.14}$$

Upon release, the initially deformed drop starts to oscillate due to the imbalanced interfacial tension forces. For drop oscillation, there is an analytical solution for the frequency of the *n*th mode of oscillation (see [31] and reference therein),

$$\omega_n = \omega_n^* - \tfrac{1}{2}\alpha\sqrt{\omega_n^*} + \tfrac{1}{4}\alpha^2, \tag{3.15}$$

where ω_n^* is Lamb's natural resonance frequency (inviscid prediction),

$$\omega_n^* = \sqrt{\frac{n(n+1)(n-1)(n+2)\sigma}{R_d^3[n\rho_g + (n+1)\rho_l]}}. \tag{3.16}$$

In equation (3.16), ρ_l and ρ_g are the densities of the *liquid* (heavy fluid) and the *gas* (light fluid). In this work, $\rho_l = \rho_g = \rho_c$, and equation (3.16) is simplified to be

$$\omega_n^* = \sqrt{\frac{n(n+1)(n-1)(n+2)\sigma}{R_d^3(2n+1)\rho_c}}. \tag{3.17}$$

In equation (3.15), the second and third terms represent the correction to ω_n^* due to viscous effects, and the parameter α is given by

$$\alpha = \frac{(2n+1)^2\rho_l\rho_g\sqrt{\nu_l\nu_g}}{\sqrt{2}R_d[n\rho_g + (n+1)\rho_l][\rho_l\sqrt{\nu_l} + \rho_g\sqrt{\nu_g}]}, \tag{3.18}$$

where ν_l and ν_g are the kinematic viscosities of the *liquid* and *gas*. In this work, $\rho_l = \rho_g = \rho_c$, $\nu_l = \nu_g = \nu$, and equation (3.18) is simplified as

$$\alpha = \frac{(2n+1)\sqrt{\nu}}{2\sqrt{2}R_d}. \tag{3.19}$$

From equations (3.15), (3.17) and (3.19), the period predicted by the inviscid theory T_n^* and the analytical period with viscous correction T_n can be calculated easily. After they are scaled by the characteristic time T_c, one can obtain the dimensionless analytical periods $\tilde{T}_n^*$ and $\tilde{T}_n$ as

$$\tilde{T}_n^* = 2\pi \frac{(2n+1)^{1/2}}{[n(n+1)(n-1)(n+2)]^{1/2}}Re^{1/2}, \tag{3.20}$$
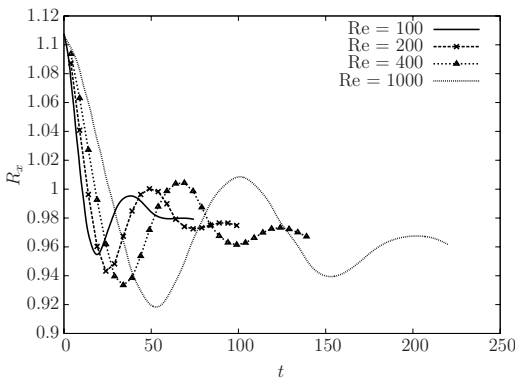
Figure 4. Comparison of the evolutions of the drop radius on the *x*-axis R_x at four different Reynolds numbers, $Re = 100, 200, 400$ and 1000, with $Ca = 1, Cn = 0.1, Pe = 4 \times 10^3, N_x = 32$ and $N_t = 256$.

$$\tilde{T}_n = 2\pi \frac{(2n+1)^{1/2}}{[n(n+1)(n-1)(n+2)]^{1/2}} Re^{1/2} \left(1 - \frac{1}{4\sqrt{2}} \frac{(2n+1)^{5/4}}{[n(n+1)(n-1)(n+2)]^{1/4}} Re^{-1/4} \right.$$
$$\left. + \frac{1}{32} \frac{(2n+1)^{5/2}}{[n(n+1)(n-1)(n+2)]^{1/2}} Re^{-1/2} \right)^{-1}. \tag{3.21}$$

As in [31], the second mode of oscillation ($n = 2$) is considered here.

The common dimensionless parameters are $Ca = 1, Cn = 0.1$ and $Pe = 4 \times 10^3$. The Reynolds number *Re* takes the following values in a series of study: 100, 125, 200, 400, 625, 1000, 2000, 4000, 6250 and 10 000. The equilibrium radius is $R_d = 1$, and the minimum and maximum radii are $R_{\min} = 0.95$ and $R_{\max} = 1.11$, respectively. The spatial and temporal discretization parameters are $N_x = 32$ and $N_y = 256$. The domain size is $L_x \times L_y = 6 \times 3$ and the center of the drop is $(x_c, y_c) = (L_x/2, 0) = (3, 0)$. The hybrid `MRT-LB-FD` method with the `iso` scheme is used. In the following, the effect of *Re* is first examined, then some comparisons with analytical solutions are provided.

The dynamically evolving drop radius on the symmetric line (the *x*-axis) R_x is examined at four different Reynolds numbers: $Re = 100, 200, 400$ and 1000. Figure 4 compares the evolutions of R_x at these *Re*. It is seen that, in accordance with the theoretical prediction, the oscillation period increases with *Re*. Besides, the amplitude of oscillation also increases with *Re* since at larger *Re*, the viscous damping effect is reduced.

Figure 5 gives the logarithmic plots of the analytical periods predicted by equations (3.20) and (3.21), $\tilde{T}_n^*$ and $\tilde{T}_n$, and the periods measured in the simulations for all the Reynolds numbers investigated. From figure 5, it is found that the viscous effect increases the period slightly, but the increment decreases as *Re* becomes higher. This is expected because the viscous effects are reduced at higher *Re*. It is also seen that the numerical prediction of the period follows the analytical one with viscous correction ($\tilde{T}_n$) quite closely. At smaller *Re*, the current method overpredicts the period (still only slightly at $Re = 100$). Such good comparisons show that the present method is able to capture the drop oscillation dynamics reasonably well with the selected numerical parameters.

3.4. Spreading drop

The next problem we consider is an initially spherical static drop near a wall which tends to spread due to the capillary force close to the surface. Note that the body force is not included
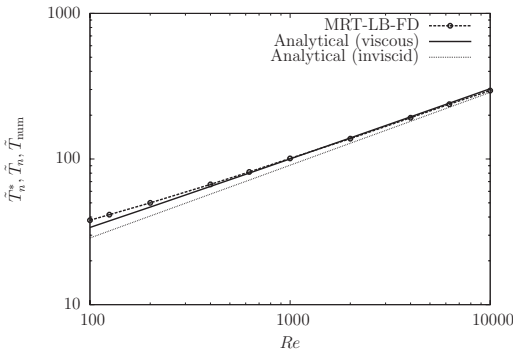
Figure 5. Comparison of the variations of the (dimensionless) analytical periods (viscous and inviscid) and the numerical period by `MRT-LB-FD` with the Reynolds number for an oscillating drop (second mode, $n = 2$). Other parameters are fixed as $Ca = 1$, $Cn = 0.1$, $Pe = 4 \times 10^3$, $N_x = 32$ and $N_t = 256$.

and the wall on which the drop spreads is located on the left side with an equilibrium contact angle $\theta_w = 90°$. The common physical parameters are $Re = 20$ and $Ca = 1$, the domain size is $L_x \times L_y = 4 \times 4$ and the initial drop center is $(x_c, y_c) = (1, 0)$. Such an initial condition corresponds to a contact angle of $180°$, which differs substantially from θ_w. It is this difference that induces large capillary force near the contact line and drives the drop to spread. The numerical parameters are $Cn = 0.1$, $Pe = 5 \times 10^3$, $N_x = 32$ and $N_t = 256$. In this problem, we focus on the evolutions of the interface and velocity field, the drop *height* on the x-axis h_x, the drop 'radius' on the (left) wall R_y (i.e. the radius of the circle on the wall formed by the contact line) and the maximum velocity magnitude $\sqrt{u^2 + v^2}|_{\max}$. Comparisons between two different methods (`MRT-LB-FD` and `NSCH-VS(FD)`) are made where appropriate.

First, we show that the drop spreading behavior is captured by the present hybrid method under the above parameters. Figure 6 gives the snapshots of the interface positions and velocity fields at selected times $t = 0, 10, 20, 30, 40$ and 50. It is observed from figure 6 that a vortex appeared near the interface in the early stage (see figure 6(*b*)) and it gradually moved away from the drop (see figures 6(*c*)–(*f*)). Note that the vortex in fact corresponds to a circular loop in three dimensions since an axisymmetric flow is studied here.

Next, we examine h_x and R_y, and $\sqrt{u^2 + v^2}|_{\max}$. Figure 7 gives the evolutions of h_x and R_y (figure 7(*a*)) and that of $\sqrt{u^2 + v^2}|_{\max}$ (figure 7(*b*)) from $t = 0$ to 100 by the hybrid `MRT-LB-FD` method, together with the corresponding evolutions by `NSCH-VS(FD)`. Again, the results by the two different methods agree quite well. As the equilibrium contact angle of the left wall is $90°$, upon reaching static equilibrium, in theory the drop should take a semispherical shape with $h_x(t \to \infty) = R_y(t \to \infty) = R_{eq}$, where R_{eq} is the radius of the final semispherical drop. From the conservation of mass, it is found that $R_{eq} = (2R^3)^{1/3} \approx 1.26$ (denoted by the horizontal line in figure 7(*a*)). In figure 7(*a*), it is observed that (under this set of parameters) h_x decreases relatively fast for $0 < t < 50$, whereas R_y keeps increasing during this stage; afterward, h_x and R_y become closer to each other (almost overlap after certain time) and their values are both quite close to the theoretical value (1.26). However, due to the specific form of free energy, the drop slowly dissolves into the ambient fluid (see [21] and references therein), which is similar to the first problem in which the drop shrinks slightly. Thus, both h_x and R_y are slightly smaller than R_{eq} and seems to keep decreasing (though at very low rates) in the final stage. This resembles the reported situation in [21]. Corresponding to the two stages of the

18
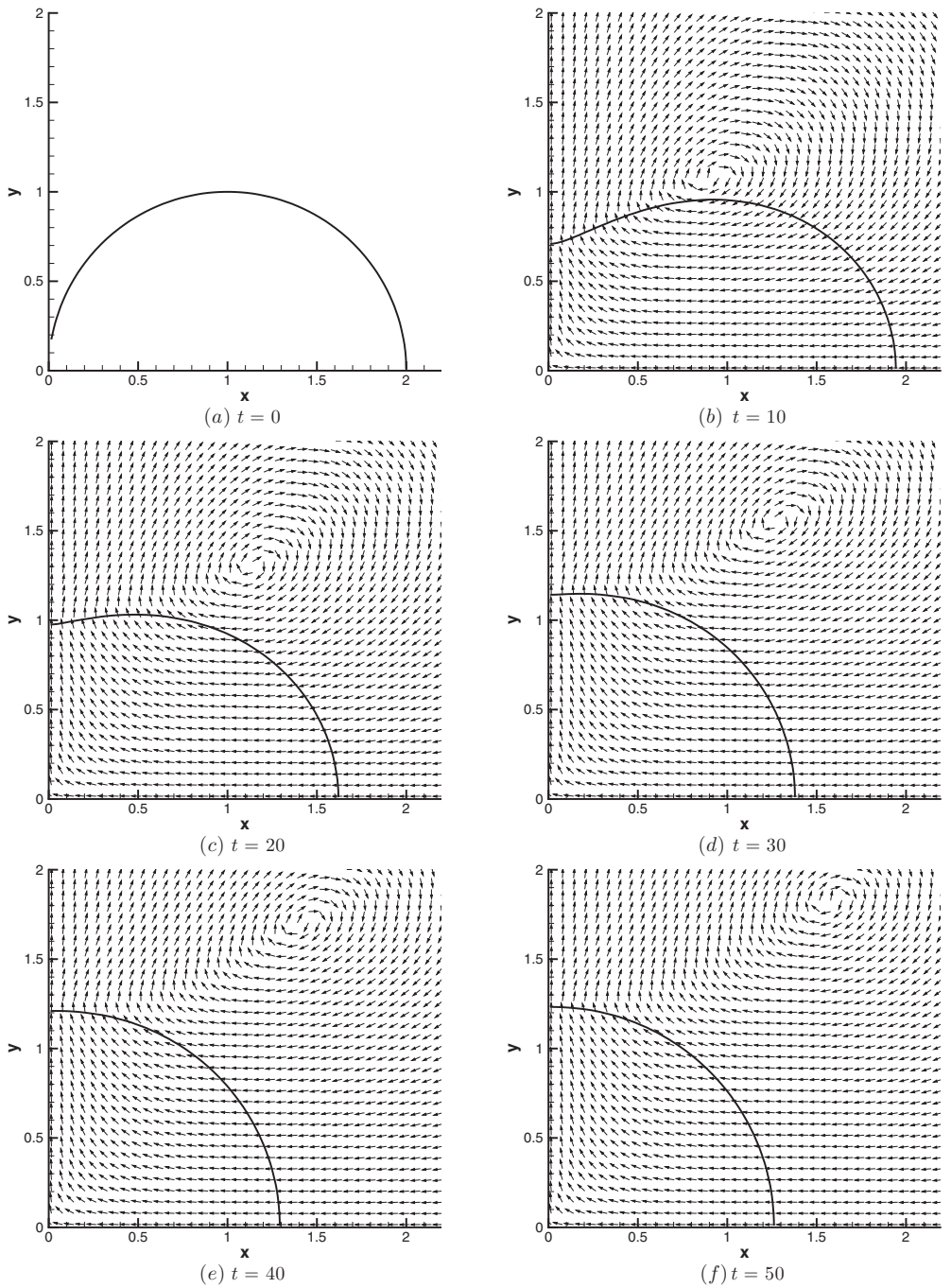
Figure 6. Snapshots of the interface and velocity field at $t = 0,\ 10,\ 20,\ 30,\ 40,\ 50$ by MRT-LB-FD with $Re = 20$, $Ca = 1$, $Cn = 0.1$, $Pe = 5 \times 10^3$, $N_x = 32$ and $N_t = 256$.
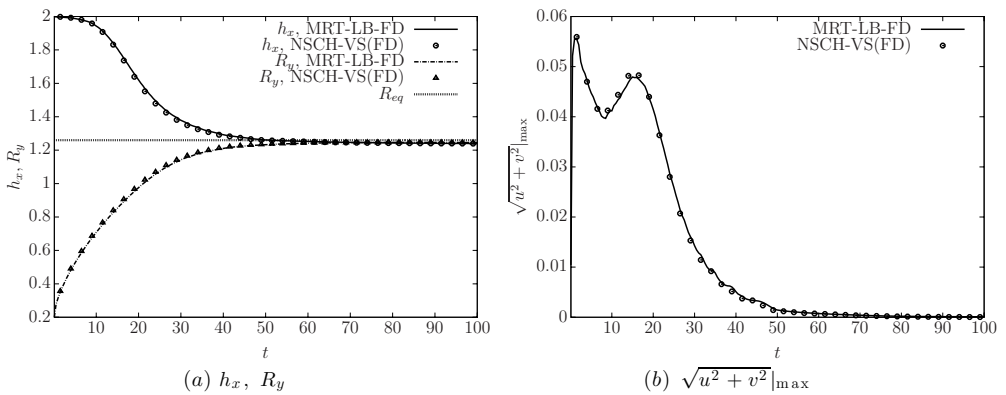
Figure 7. Comparison of the evolutions of (*a*) the drop height on the *x*-axis h_x and the drop 'radius' on the (left) wall R_y (*b*) the maximum velocity magnitude $\sqrt{u^2 + v^2}|_{\max}$ by MRT-LB-FD and NSCH-VS(FD) with $Re = 20$, $Ca = 1$, $Cn = 0.1$, $Pe = 5 \times 10^3$, $N_x = 32$ and $N_t = 256$.
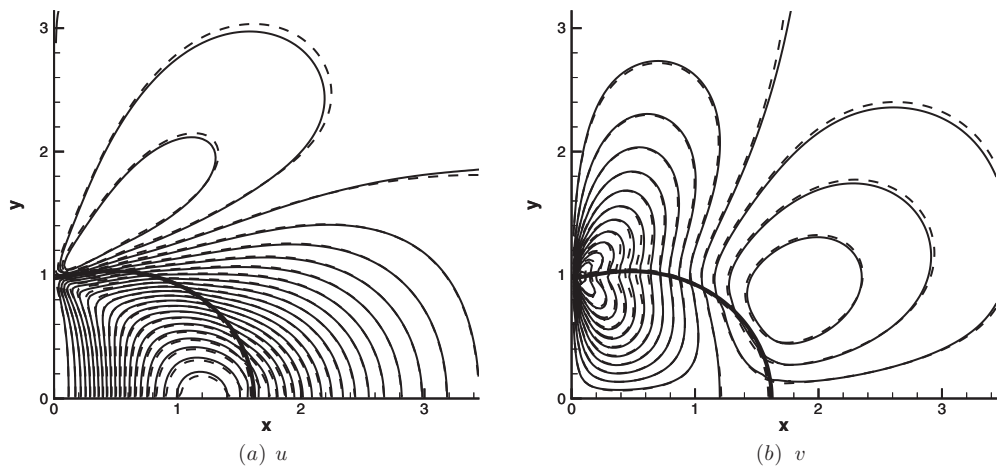
Figure 8. Comparison of the contours of (*a*) the velocity component *u* and (*b*) the velocity component *v* at $t = 20$ by MRT-LB-FD (solid lines) and NSCH-VS(FD) (dashed lines) with $Re = 20$, $Ca = 1$, $Cn = 0.1$, $Pe = 5 \times 10^3$, $N_x = 32$ and $N_t = 256$. The interfaces are shown in thicker lines (the small difference of the interface between the two methods is hard to see because of the line thickness).

evolutions of h_x and R_y, it is seen from figure 7(*b*) that $\sqrt{u^2 + v^2}|_{\max}$ remains to be relatively large (of order $O(10^{-2})$) for $0 < t < 50$ and decays very fast afterward (of order $O(10^{-4})$ at $t = 100$) as the system gradually approaches its static equilibrium.

To make the comparison more comprehensive, we examine the velocity components *u* and *v* at one selected moment with significant macroscopic flow ($t = 20$) by the present method and by NSCH-VS(FD). Figure 8 shows the contours of *u* (figure 8(*a*)) and *v* (figure 8(*b*)) at $t = 20$. It is found that overall the two methods give velocity fields that are quite close to each other. At the same time, some notable differences are observed in regions far away from the drop, but they do not seem to be significant and indeed they do not lead to substantial differences in subsequent drop motions (as manifested through figure 7).
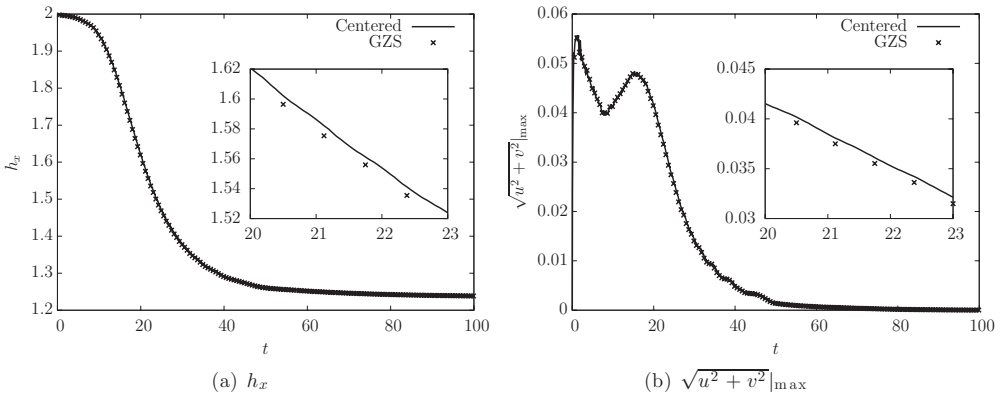
Figure 9. Comparison of the evolutions of (*a*) the drop height on the *x*-axis h_x and (*b*) the maximum velocity magnitude $\sqrt{u^2 + v^2}|_{max}$ during drop spreading by the hybrid MRT-LB-FD method with different forcing schemes ('centered' and 'GZS') with $Re = 20$, $Ca = 1$, $Cn = 0.1$, $Pe = 5 \times 10^3$, $N_x = 32$ and $N_t = 256$.

It was noted in section 2.2.2 that the two forcing formulations ('GZS' based on [8] and 'centered' based on [11, 43]) give results that are very close to each other. Here, some detailed comparisons are given for a drop spreading on a wall with the above parameters ($Re = 20$, $Ca = 1$, $Cn = 0.1$, $Pe = 5 \times 10^3$, $N_x = 32$ and $N_t = 256$). Figure 9 compares the evolutions of the drop height on the *x*-axis h_x (figure 9(*a*)) and the maximum velocity magnitude $\sqrt{u^2 + v^2}|_{max}$ (figure 9(*b*)) computed using these two formulations. It is seen that h_x and $\sqrt{u^2 + v^2}|_{max}$ obtained by using them almost overlap when one observes at a large scale; only when the plots are zoomed in (see the insets in figure 9) can some small differences be noted. The small differences between the two forcing formulations were also observed for some other cases like the drop accelerated by a constant body force to be discussed in section 3.5 (for conciseness, comparisons for other cases will not be shown). According to Guo *et al* [8], the macroscopic equations recovered from the LBEs using the 'centered' formulation [11] contain some extra terms related to the force, the time step and the velocity, which would cause certain deviations from the accurate solutions in the presence of variable forces; by contrast, the 'GZS' formulation is free of such extra terms. Based on our tests, the effects of the extra terms seem to be minor here. This may be due to the following reasons: (a) the binary fluid simulations usually require small time steps (because of the property of the CHE), thus making the discrete effects less important; (b) the interfacial tension forces are effective only in a limited, small region (i.e. the interfacial region), instead of the whole field; (c) the velocity is in general (required to be) small to ensure stable computations.

3.5. Drop accelerated by a constant body force

The last problem is on a drop accelerated by a constant body force. This problem differs from the above ones in several aspects, probably the most important of which is that it has significant flow. In this problem, a drop with a density ρ_d and dynamic viscosity η_d is surrounded by another fluid with a density ρ_o and dynamic viscosity η_o. The whole fluid is subject to a constant body force along the *x*-(*z*-)direction with its magnitude being a_z. Denote the density ratio as $r_\rho = \rho_d/\rho_o$ and the (dynamic) viscosity ratio as $r_\eta = \eta_d/\eta_o$. Besides these two dimensionless

21

parameters, two other parameters are important in this problem. They are the Eötvös number (also known as the Bond number) and the Ohnesorge number (of the drop) [10]:

$$\text{Eo} = \frac{a_z \Delta \rho D^2}{\sigma}, \quad \text{Oh}_d = \frac{\eta_d}{\sqrt{\rho_d D \sigma}}, \tag{3.22}$$

where $\Delta \rho = \rho_d - \rho_o$ is the density difference and $D(= 2R)$ is the (initial) diameter of the drop.

Based on the properties of the surrounding fluid, another Ohnesorge number [10] can be defined as

$$\text{Oh}_o = \frac{\eta_o}{\sqrt{\rho_o D \sigma}}, \tag{3.23}$$

which is related to Oh_d as $\text{Oh}_o = (\sqrt{r_\rho}/r_\eta)\text{Oh}_d$. If we use the drop properties to define those characteristic quantities ($L_c = R$, $U_c = \sigma/\eta_d$) and dimensionless numbers ($Re(= We) = \frac{\rho_d U_c R}{\eta_d}$) in section 3.1, we find that those parameters are related to the newly introduced parameters as

$$Re(= We) = \frac{1}{\sqrt{2}\text{Oh}_d^2}, \quad \text{Eo} = 4\left(1 - \frac{1}{r_\rho}\right)a_z^* We, \tag{3.24}$$

where $a_z^* = a_z/(U_c^2/L_c)$ is the scaled body force magnitude. In addition, based on a_z and D, another characteristic velocity U_c' and another characteristic time T_c' may be defined as

$$U_c' = \sqrt{a_z D}, \quad T_c' = \sqrt{D/a_z}, \tag{3.25}$$

which are related to U_c and T_c as

$$U_c' = \sqrt{2a_z^*}U_c, \quad T_c' = \sqrt{2/a_z^*}T_c. \tag{3.26}$$

In what follows, the velocity and time are measured in U_c' and T_c' (instead of U_c and T_c), respectively. Using the order parameter field ϕ, the density and (dynamic) viscosity may be expressed as

$$\rho(\phi) = \tfrac{1}{2}[\rho_d(1+\phi) + \rho_o(1-\phi)], \quad \eta(\phi) = \tfrac{1}{2}[\eta_d(1+\phi) + \eta_o(1-\phi)]. \tag{3.27}$$

When the density difference is small (i.e. r_ρ is close to unity), one may employ the Boussinesq approximation to deal with such problems [10, 24]. For completeness, the momentum equation using the Boussinesq approximation is briefly derived as follows.

The original momentum equation in a vector form for two-phase flows with variable density and viscosity and subject to a constant body force in the z-direction may be written as

$$\rho(\phi)\left(\frac{\partial \boldsymbol{u}}{\partial t} + (\boldsymbol{u} \cdot \nabla)\boldsymbol{u}\right) = -\nabla S_p + \nabla \cdot [\eta(\phi)(\nabla \boldsymbol{u} + (\nabla \boldsymbol{u})^T)] + \boldsymbol{F}_{ST} + \rho(\phi)a_z \boldsymbol{e}_z, \tag{3.28}$$

where $\boldsymbol{e}_z$ denotes the unit vector in the z-direction. We are interested about the state in which the drop only occupies a small portion of the whole field and the whole field is not far away from its static equilibrium, under which the pressure is simply the hydrostatic pressure. Then, one may rewrite the momentum equation as (see [24] for a similar but slightly different derivation)

$$\rho(\phi)\left(\frac{\partial \boldsymbol{u}}{\partial t} + (\boldsymbol{u} \cdot \nabla)\boldsymbol{u}\right) = -\nabla(S_p - \rho_o a_z(z + z_0)) + \nabla \cdot [\eta(\phi)(\nabla \boldsymbol{u} + (\nabla \boldsymbol{u})^T)]$$
$$+ \boldsymbol{F}_{ST} + (\rho(\phi) - \rho_o)a_z \boldsymbol{e}_z, \tag{3.29}$$

where z_0 is a constant and may be safely neglected. Let $S_p' = S_p - \rho_o a_z(z + z_0)$ (i.e. we are concerned about the deviation from the static equilibrium). After one replaces $\rho(\phi)$ on the

left-hand side with the average density $\overline{\rho} = (\rho_d + \rho_o)/2$ (justified when r_ρ is close to unity), one obtains the following momentum equation:

$$\overline{\rho}\left(\frac{\partial \boldsymbol{u}}{\partial t} + (\boldsymbol{u} \cdot \nabla)\boldsymbol{u}\right) = -\nabla S'_p + \nabla \cdot [\eta(\phi)(\nabla \boldsymbol{u} + (\nabla \boldsymbol{u})^T)] + \boldsymbol{F}_{\text{ST}} + (\rho(\phi) - \rho_o)a_z\boldsymbol{e}_z. \tag{3.30}$$

In addition, in the specific case considered below, the dynamic viscosity is uniform. Then, equation (3.30) may be further simplified as (*note*: also using the incompressibility condition $\nabla \cdot \boldsymbol{u} = 0$)

$$\overline{\rho}\left(\frac{\partial \boldsymbol{u}}{\partial t} + (\boldsymbol{u} \cdot \nabla)\boldsymbol{u}\right) = -\nabla S'_p + \eta\nabla^2\boldsymbol{u} + \boldsymbol{F}_{\text{ST}} + (\rho(\phi) - \rho_o)a_z\boldsymbol{e}_z. \tag{3.31}$$

Thus, the present governing equations (equations (2.13) and (2.14)) are still applicable once the body force is included and a simple scaling is carried out (though, of course, with certain approximations).

The setup for this problem is as follows. On the upper side, the free slip boundary condition is applied (for f_i), and on the left and right sides, the periodic boundary condition is used (for f_i). In addition, in this problem the interfaces are always (ensured to be) away from these three sides. Therefore, the *zero-normal-gradient* condition can be applied for both ϕ and μ as well. Initially, the drop is spherical, located on the axis near the left side, and there is no flow anywhere. Under the action of the body force, the drop is accelerated gradually and moves along the axis (in the z-direction).

We mainly investigate one case using the proposed hybrid MRT-LB-FD method and compare the present results with those given by Han and Tryggvason [10]. In [10], the front-tracking method [39] was employed to treat the interface and the (original) NSEs for flows with variable density and viscosity were solved by an FDM (thus that work is denoted as NS-FT-FD). It is noted that the results in [10] were well validated and compared favorably with experimental results (for even more cases besides the one selected here). The specific physical parameters are as follows: Eo = 144, $\text{Oh}_d = 0.0466$, $r_\rho = 1.15$ and $r_\eta = 1$ (giving $\text{Oh}_o = 0.05$). All physical parameters are chosen to match one specific case in [10] with abundant data for comparison and also within the capability of the present model (to allow the use of the Boussinesq approximation).

During the simulation, two dynamic quantities are monitored: (a) the aspect ratio of the drop, denoted by α and defined to be the drop thickness along the axis (in the x-(z-)direction) over the maximum drop width (in the y-(r-)direction); (b) the centroid velocity of the drop in the x-(z-)direction V_c which is calculated by

$$V_c = \frac{\int_{A|_{\phi>0}} r u(r, z)\, \mathrm{d}r\, \mathrm{d}z}{\int_{A|_{\phi>0}} r\, \mathrm{d}r\, \mathrm{d}z} \approx \frac{\sum_{i,j|_{\phi_{i,j}>0}} r_{i,j} u_{i,j}}{\sum_{i,j|_{\phi_{i,j}>0}} r_{i,j}}, \tag{3.32}$$

where $A|_{\phi>0}$ denotes the region where $\phi > 0$. Other parameters are $Cn = 0.06$, $Pe = 1000$, $N_x = 50$ and $N_t = 2000$, the domain size is $L_x \times L_y = 24 \times 8$ and the initial drop position is $(x_c, y_c) = (2, 0)$.

Figure 10 compares the evolutions of α and V_c for $0 \leqslant t' \leqslant 15$ (*note*: t' is measured in T'_c) with those in [10]. The data of [10] were extracted from its figure 3 (obtained on the finest grid). From figure 10, it can be seen that the present evolutions of α and V_c follow closely the reference ones for most of the time. Some deviations are observed in the later stage. This could be caused by the small thickness of the drop at the later stage. If fact, based on [10, figure 3(a)], α becomes zero (due to zero thickness) at about $t' = 20$, but in the present simulation, this occurred at about $t' = 12$ (see figure 10(*a*)). Small thickness means the top and bottom sides of the drop (or the left and right sides under the present coordinate setting) on the axis are

(a) Aspect ratio α (b) Centroid velocity V_c
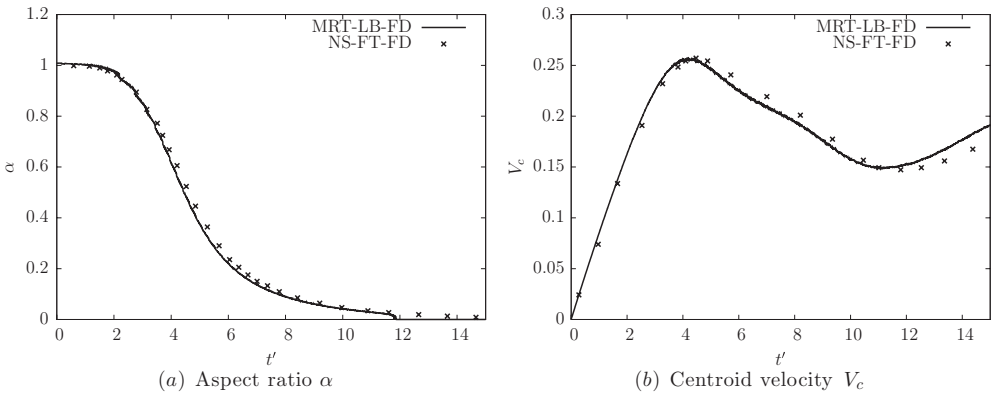
Figure 10. Comparison of the evolutions of (*a*) the aspect ratio α of the drop and (*b*) the centroid velocity V_c of the drop by the present `MRT-LB-FD` method and the `NS-FT-FD` method [10] with Eo = 144, $Oh_d = 0.0466$ ($Oh_o = 0.05$), $r_\rho = 1.15$ and $r_\eta = 1$. The numerical parameters are $Cn = 0.06$, $Pe = 1000$, $N_x = 50$ and $N_t = 2000$.

very close to each other and it becomes difficult to resolve the details in that region. Because of the intrinsic diffusion around the interfaces in the phase-field modeling, the two sides tend to merge more easily than in the front-tracking method (for which topological changes such as interface merging and breakup must be manually treated). This merging should also depend on the interface thickness (or *Cn*). This work uses a uniform grid, whereas a stretched grid was used in [10], allowing better resolution for the interfaces (thus delayed merging). These factors may explain the early occurrence of zero α in figure 10. Besides, this work employs the Boussinesq approximation, which may also contribute to the differences to some degree.

Nevertheless, we would argue that despite the significant differences in the model, method and numerical parameters, this work has shown quite good agreement with [10] (when the resolution of the interface is enough, e.g., for $0 \leqslant t' \leqslant 12$). This is also supported by the well-captured drop shapes and flow fields at certain times. Figure 11 shows the snapshots of the interfaces and the flow fields around the drop at three selected times ($t' = 3.87,\ 7.73,\ 11.60$). These moments to take the snapshots are chosen to match [10, figure 9]. Note that for easy comparison with [10], the plots have been rotated so that the *x*-(*z*-)direction now points downward. Also note that the velocities in the *x*-(*z*-)direction are relative to the drop (i.e. $u - V_c$) at each moment. In other words, the plots present what one observes when moving with the drop at its centroid velocity V_c. It is seen from figure 11 that the deformation of the drop increases gradually with time, from an intermediate degree at $t' = 3.87$ (see figure 11(*a*)) to a very high degree at $t' = 11.60$ (see figure 11(*c*)). Besides, in the reference frame moving with the drop, the streamlines are deformed around the drop with the configurations largely conforming to the instantaneous drop shape in the upstream, and a circulation region exists on/near the drop with the streamlines passing through the interface downstream (see figure 11(*a*)) or the whole drop (see figures 11(*b*) and (*c*)) (depending on the degree of drop deformation). All these observations, including the drop shape and streamline pattern, are very similar to those reported in [10] (see figure 9 therein) although the second selected time differs very slightly ($t' = 7.75$ in [10] instead of 7.73 here).

(*a*) $t' = 3.87$

(*b*) $t' = 7.73$

(*c*) $t' = 11.60$
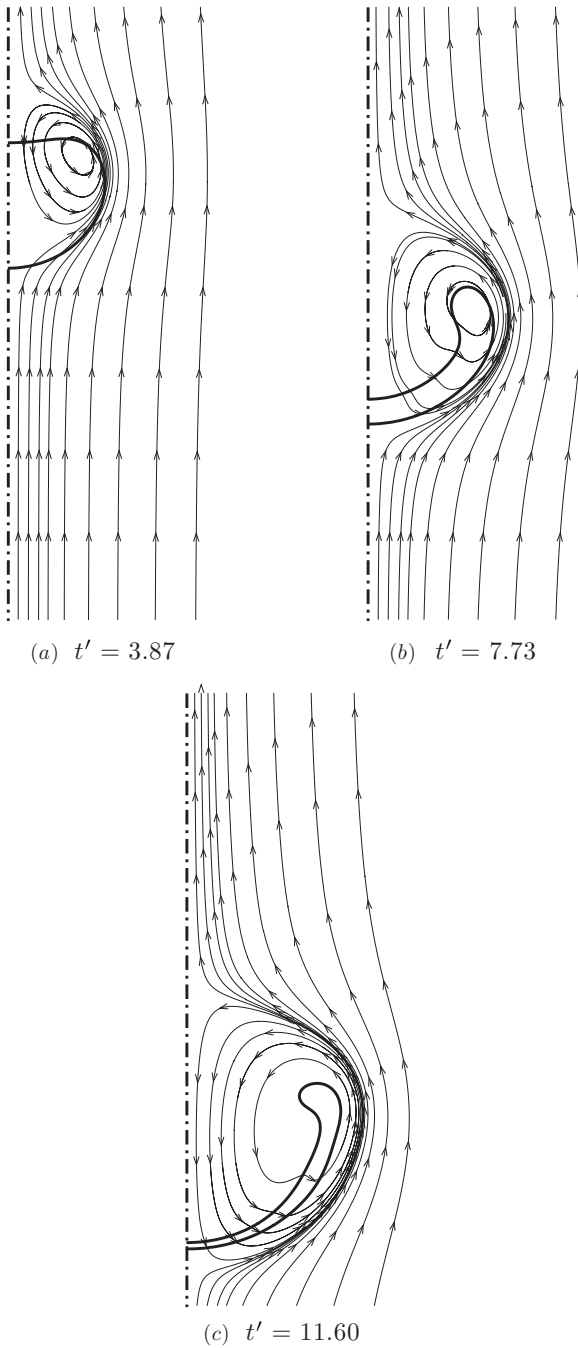
Figure 11. Snapshots of the interfaces (in thicker lines) and the flow fields around the drop (displayed in streamlines with arrows indicating the flow directions) at three selected times with Eo = 144, $\mathrm{Oh}_d = 0.0466$, $r_\rho = 1.15$ and $r_\eta = 1$ ($\mathrm{Oh}_o = 0.05$). The left vertical line is the axis.

4. Concluding remarks

To summarize, a hybrid MRT lattice-Boltzmann finite-difference numerical method based on the phase-field theory has been developed for axisymmetric binary fluids. It has been shown to be able to simulate several axisymmetric drop problems, involving interactions with ambient fluid and/or a solid wall, or involving motions under a constant body force. The obtained results were compared favorably with analytical solutions or other solutions by directly solving the NSEs with the phase-field or front-tracking methods to treat interfaces [18, 10]. Besides, for the hydrodynamics simulated by the LBEs, the MRT collision model is much more stable than SRT, and is thus preferred. Two formulations to apply the forcing, based on [11, 43] and [8], respectively, were considered and implemented in the present hybrid MRT-LB-FD framework and compared with each other. No significant differences were found between them and the simpler one based on [11, 43] was chosen as the default. For the CHE that captures interface motions, a comparison between the central second-order scheme and the isotropic scheme based on the D2Q9 lattice velocity model shows that the latter is better. This hybrid method is free from some issues concerning the previous LBM using double DFs and it preserves the benefits of using the LBM for hydrodynamics. Thus, it may be a good alternative to the existing LBM for the simulation of complex axisymmetric multiphase flows.

Acknowledgments

References

[1] Anderson D M, McFadden G B and Wheeler A A 1998 Diffuse-interface methods in fluid mechanics *Annu. Rev. Fluid Mech.* **30** 139

[2] Badalassi V E, Ceniceros H D and Banerjee S 2003 Computation of multiphase systems with phase field models *J. Comput. Phys.* **190** 371–97

[3] Briant A J and Yeomans J M 2004 Lattice Boltzmann simulations of contact line motion: II. Binary fluids *Phys. Rev.* E **69** 031603

[4] Chang Y C, Hou T Y, Merriman B and Osher S 1996 A level set formulation of Eulerian interface capturing methods for incompressible fluid flows *J. Comput. Phys.* **124** 449

[5] Chen S and Doolen G D 1998 Lattice Boltzmann method for fluid flows *Annu. Rev. Fluid Mech.* **30** 329

[6] Fakhari A and Rahimian M H 2010 Phase-field modeling by the method of lattice Boltzmann equations *Phys. Rev.* E **81** 036707

[7] Gonnella G, Lamura A, Piscitelli A and Tiribocchi A 2010 Phase separation of binary fluids with dynamic temperature *Phys. Rev.* E **82** 046302

[8] Guo Z, Zheng C and Shi B 2002 Discrete lattice effects on the forcing term in the lattice Boltzmann method *Phys. Rev.* E **65** 46308

[9] Halliday I, Hammond L A, Care C M, Good K and Stevens A 2001 Lattice Boltzmann equation hydrodynamics *Phys. Rev.* E **64** 11208

[10] Han J and Tryggvason G 1999 Secondary breakup of axisymmetric liquid drops: I. Acceleration by a constant body force *Phys. Fluids* **11** 3650–67

[11] He X, Zou Q, Luo L-S and Dembo M 1997 Analytic solutions of simple flows and analysis of nonslip boundary conditions for the lattice Boltzmann BGK model *J. Stat. Phys.* **87** 115–36

[12] Henrich O, Marenduzzo D, Stratford K and Cates M E 2010 Domain growth in cholesteric blue phases: hybrid lattice Boltzmann simulations *Comput. Math. Appl.* **59** 2360–9

[13] Huang H, Krafczyk M and Lu X 2011 Forcing term in single-phase and Shan–Chen-type multiphase lattice Boltzmann models *Phys. Rev.* E **84** 046710

[14] Huang H, Lee T S and Shu C 2007 Hybrid lattice Boltzmann finite-difference simulation of axisymmetric swirling and rotating flows *Int. J. Numer. Methods Fluids* **53** 1707–26

[15] Huang H and Lu X-Y 2009 Theoretical and numerical study of axisymmetric lattice Boltzmann models *Phys. Rev.* E **80** 016701

[16] Huang J J, Shu C and Chew Y T 2009 Mobility-dependent bifurcations in capillarity-driven two-phase fluid systems by using a lattice Boltzmann phase-field model *Int. J. Numer. Methods Fluids* **60** 203–25

[17] Huang J J, Shu C, Feng J J and Chew Y T 2012 A phase-field-based hybrid lattice-Boltzmann finite-volume method and its application to simulate droplet motion under electrowetting control *J. Adhes. Sci. Technol.* **26** 1825–51

[18] Huang J-J, Huang H and Wang S-L 2012 Numerical method for axisymmetric simulation of binary fluids based on phase-field theory and vorticity-stream function formulation *Int. J. Numer. Methods Fluids* submitted

[19] Jacqmin D 1999 Calculation of two-phase Navier–Stokes flows using phase-field modeling *J. Comput. Phys.* **155** 96

[20] Kendon V M, Cates M E, Pagonabarraga I, Desplat J-C and Bladon P 2001 Inertial effects in three-dimensional spinodal decomposition of a symmetric binary fluid mixture: a lattice Boltzmann study *J. Fluid Mech.* **440** 147

[21] Khatavkar V V, Anderson P D and Meijer H E H 2007 Capillary spreading of a droplet in the partially wetting regime using a diffuse-interface model *J. Fluid Mech.* **572** 367

[22] Lallemand P and Luo L-S 2000 Theory of the lattice Boltzmann method: dispersion, dissipation, isotropy, Galilean invariance, and stability *Phys. Rev.* E **61** 6546

[23] Lallemand P and Luo L-S 2003 Theory of the lattice Boltzmann method: acoustic and thermal properties in two and three dimensions *Phys. Rev.* E **68** 036706

[24] Lee H G and Kim J 2012 A comparison study of the Boussinesq and the variable density models on buoyancy-driven flows *J. Eng. Math.* **75** 15–27

[25] Lee T and Lin C-L 2005 A stable discretization of the lattice Boltzmann equation for simulation of incompressible two-phase flows at high density ratio *J. Comput. Phys.* **206** 16

[26] Mezrhab A, Bouzidi M and Lallemand P 2004 Hybrid lattice-Boltzmann finite-difference simulation of convective flows *Comput. Fluids* **33** 623–41

[27] Moussaoui M A, Jami M, Mezrhab A and Naji H 2009 Convective heat transfer over two blocks arbitrary located in a 2D plane channel using a hybrid lattice Boltzmann-finite difference method *Heat Mass Transfer* **45** 1373–81

[28] Mukherjee S and Abraham J 2007 Lattice Boltzmann simulations of two-phase flow with high density ratio in axially symmetric geometry *Phys. Rev.* E **75** 026701

[29] Niu X-D, Munekata T, Hyodo S-A and Suga K 2007 An investigation of water–gas transport processes in the gas-diffusion-layer of a PEM fuel cell by a multiphase multiple-relaxation-time lattice Boltzmann model *J. Power Sources* **172** 542–52

[30] Peng Y, Shu C, Chew Y T and Qiu J 2003 Numerical investigation of flows in Czochralski crystal growth by an axisymmetric lattice Boltzmann method *J. Comput. Phys.* **186** 295–307

[31] Premnath K N and Abraham J 2005 Lattice Boltzmann model for axisymmetric multiphase flows *Phys. Rev.* E **71** 056706

[32] Reis T and Philips T N 2007 Modified lattice Boltzmann model for axisymmetric flows *Phys. Rev.* E **75** 056703

[33] Scardovelli R and Zaleski S 1999 Direct numerical simulation of free-surface and interfacial flow *Annu. Rev. Fluid Mech.* **31** 567

[34] Succi S 2001 *The Lattice Boltzmann Equation for Fluid Dynamics and Beyond* (New York: Clarendon)

[35] Swift M R, Orlandini E, Osborn W R and Yeomans J M 1996 Lattice Boltzmann simulations of liquid–gas and binary fluid systems *Phys. Rev.* E **54** 5041

[36] Swift M R, Osborn W R and Yeomans J M 1995 Lattice Boltzmann simulation of nonideal fluids *Phys. Rev. Lett.* **75** 830

[37] Tiribocchi A, Stella N, Gonnella G and Lamura A 2009 Hybrid lattice Boltzmann model for binary fluid mixtures *Phys. Rev.* E **80** 026701

[38] Tiribocchi A, Piscitelli A, Gonnella G and Lamura A 2011 Pattern study of thermal phase separation for binary fluid mixtures *Int. J. Numer. Methods Heat Fluid Flow* **21** 572–83

[39] Unverdi S O and Tryggvason G 1992 A front-tracking method for viscous, incompressible, multi-fluid flows *J. Comput. Phys.* **100** 25

[40] Yue P, Zhou C and Feng J J 2007 Spontaneous shrinkage of drops and mass conservation in phase-field simulations *J. Comput. Phys.* **223** 1

[41] Yue P, Zhou C and Feng J J 2010 Sharp-interface limit of the Cahn–Hilliard model for moving contact lines *J. Fluid Mech.* **645** 279–94

[42] Zheng H W, Shu C and Chew Y T 2006 A lattice Boltzmann model for multiphase flows with large density ratio *J. Comput. Phys.* **218** 353–71

[43] Zhou J G 2008 Axisymmetric lattice Boltzmann method *Phys. Rev.* E **78** 036701

[44] Zou Q and He X 1997 On pressure and velocity boundary conditions for the lattice Boltzmann BGK model *Phys. Fluids* **9** 1591–8